Investigating Ground and Obstacle Effects on the Aerodynamics of UAM Aircraft in Full Configuration

Chan Ho Song, Gyeongsang National University, Jinju, Republic of Korea
Sang Min Son, Gyeongsang National University, Jinju, Republic of Korea
Da-bin Jung, Gyeongsang National University, Jinju, Republic of Korea
Rho Shin Myong, Gyeongsang National University, Jinju, Republic of Korea
Hakjin Lee, Gyeongsang National University, Jinju, Republic of Korea

Abstract

Urban Air Mobility (UAM) has emerged as a solution to mitigate urban traffic congestion, and it is expected to operate congested environment with various obstacles, such as vertiports and surrounding buildings. However, these environments can produce unsteady aerodynamic interferce phenomea, including ground and obstacle effects, which may increase the risk of accidents. In this study, the obstacle effects on the aerodynamic performance and wake structure of a side-by-side UAM aircraft in full configuration are investigated using the vortex-based rotorcraft analysis code VALOR (Vortex-based Aerodynamic simuLation cOde for Rotorcraft). The simulation results indicate that the presence of obstacles causes the distortion of wake structure, which directly influences azimuthal variaion in the aerodynamic loads acting on the rotor blade. As the UAM aircraft approaches the obstacle, the induced velocity decreases, which results in increased thrust compared to the out-of-ground-effect condition. Based on the parametric study, the obstacle effect becomes most dominant when the aircraft is near or above the obstacle. The findings in this study help to establish safe operating guidelines for take-off and landing of UAM aircraft.

1. NOTATION

Symbols

R	Rotor radius, m
D	Rotor diameter, m
ψ	Azimuth angle, deg
C_T	Thrust coefficient
σ	Source strength
μ	Doublet strength

Acronyms:

UAM	Urban Air Mobility
CFD	Computational Fluid Dynamics
IGE	In-ground Effects
OGE	Out-of-ground Effects
VPM	Vortex Particle Method
CW	Clockwise Rotation
CCW	Counterclockwise Rotation
FATO	Final Approach and Take-off Area

2. INTRODUCTION

Urban Air Mobility (UAM) is a new transportation system designed for passenger and cargo transport in urban environments, is being accelerated as a solution to alleviate urban traffic congestion. During the vertical takeoff and landing operation in urban areas, UAM aircraft interact with obstacles such as buildings, helipads located on rooftops, and vertiports. In these operation, aerodynamic interactions occur between the wake generated by the rotor and surrounding obstacles, leading to degradation of aircraft performance, flight instability, and high compensatory workload for the pilot (Ref. 1). As UAM primarily operates in urban environments or at low altitudes over short distances between cities, it is more susceptible to complex aerodynamic interactions compared to other rotary-wing aircraft (Ref. 2). Therefore, Investigating the impact of ground and obstacle effects on a UAM aircraft is imperative to ensure safe operation and to avoid accidents that may occur during vertical take-off and landing.

Ground and Obstacle effect influences rotorcraft performance due to the presence of a boundary inhibiting rotor wake development. When a helicopter or UAM aircraft hovers near the ground plane, the ground effect increases rotor thrust at the same power (Ref. 3,4). In addition, the rotor wake initially propagates downward but expands rapidly as it approaches the ground. This expansion changes the flow from vertical downwash into radial outwash, developing a radial wall jet that alters induced and slipstream velocities (Ref. 5). When operating near obstacles such as buildings and vertiports, the obstacle effects must be considered. The rotor wake is reflected by the ground and the obstacle surfaces, forming a recirculation region. This region produces unsteady loads on the rotor, which can lead to control instability and blade vibration (Ref. 6). Since strong interactions caused by ground and obstacle effects can directly lead to flight instability and potential accidents, it is important to predict the international aerodynamics of rotorcraft operating near obstacles to ensure safe operation.

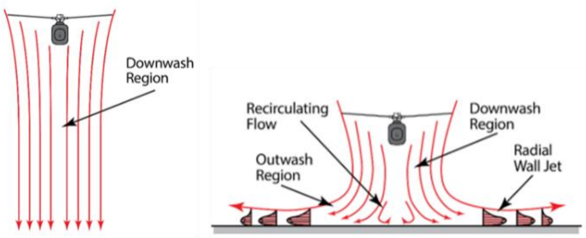

(a) (b)

Figure 1: Wake from a hovering rotor: (a) out of ground effect (OGE); (b) in ground effect (IGE) (Ref. 7)

Several studies have previously investigated the influence of ground and obstacle effects on the performance of Isolated rotor or helicopters through computational and experimental approaches. Zagaglia et al. (Ref. 8) conducted experiments at various positions near the ground and obstacles to analyze the aerodynamics and wake structure of a single rotor blade. Chirico et al. (Ref. 9) employed the Computational Fluid Dynamics (CFD) solver HMB to analyze the velocity field between the rotor and obstacles. The European aeronautical research and technology group, Aeronautical Research and Technology in Europe (GARTEUR AG22), has been conducting research under the project "Forces on Obstacles in Rotor Wake" to develop an experimental database and efficient numerical models aimed at analyzing complex wake interactions between helicopters and obstacles (Ref. 10). Additionally, several reasearch group recently investigated the ground effect on the side-by-side rotor's performance and aerodynamics. Sagaga and Lee (Ref. 11) conducted a high-fidelity computational study of a side-by-side rotor under in-ground effect(IGE) conditions to analyze the flow physics and aerodynamic characteristics. They found that as the overlap increased, the influence of the ground surface on rotor performance decreased. However, the fuselage was not included in their side-by-side rotor configuration. Sadegh et al. (Ref. 12) investigated the effects of fuselage and ground on the aerodynamic performance of side-by-side UAM aircraft in full configuration using the coupled vortex method. They identified that as the UAM aircraft approaches the ground, the impact of the fuselage becomes more noticeable due to the stronger upwash wake by the airframe and the ground. Although numerous studies have investigated side-by-side UAM aircraft under IGE conditions, most of them were conducted using simplified geometries such as a flat ground surface.

However, as UAM aircraft are expected to operate frequently within urban environments, it is essential to analyze the aerodynamics and wake behavior in such environments. Also, to ensure the stable introduction and operation of UAM, continuous studies on ground and obstacle effects, considering urban environments, are required. Most previous studies have primarily performed experimental or CFD analysis methods. However, predicting the asymmetric and unsteady behavior of the wake flow field affected by ground and obstacle effects requires a high computational cost. Additionally, since the effect of ground and obstacle vary depending on the aircraft's position, a large number of parametric studies are necessary for a detailed analysis of these interactions. Therefore, the objective of this work is to numerically study the interactional aerodynamics and wake behavior of a full configuration of side-by-side UAM aircraft in the vicinity of an obstacle. An In-house code that combines the source–doublet panel method and the unsteady vortex particle method(VPM) is used for the analysis. To validate the numerical method used in this study, the aerodynamic performance and tip vortex particle trajectories influenced by ground and obstacle effects were predicted using the Lynx tail rotor and MD-500 model. In addition, a parametric study was conducted using a side-by-side UAM aircraft in full configuration to examine the effects of ground and obstacle on aerodynamic performance and wake behavior.

3. NUMERICAL METHODOLOGY

3.1 Source-Doublet Panel Method

In this study, the In-house code called the VALOR (Vortex-based Aerodynamic simuLation cOde for Rotorcraft), a vortex-based rotorcraft analysis software, was used to calculate the aerodynamic loads acting on the rotor blades. The aerodynamic analysis model is based on the Source-doublet panel method, which employs rectangular source-doublet panels to model the surface of the three-dimensional rotor blade. Unlike the Vortex Lattice Method (VLM), it is possible to consider thickness, allowing for a more accurate representation of the geometric characteristics of complex three-dimensional rotor blades. Also, not only the rotor blades but also the ground and obstacles were modeled using the source-doublet panels with constant-strength. The flow is assumed to be inviscid, incompressible, or irrotational, the continuity equation can be expressed as the Laplace equation in terms of the velocity potential (Ref. 13,14). The velocity potential function is defined as the sum of the source (σ) and doublet (μ) distributions over the body surface and wake panel, as expressed in Eq. (1).

$$\phi_i^*(x) = -\frac{1}{4\pi}\oiint_{S_B}[\sigma\left(\frac{1}{r}\right) - \mu\nabla\left(\frac{1}{r}\right)\cdot\mathbf{n}]dS + \frac{1}{4\pi}\oiint_{S_W}\mu\nabla\left(\frac{1}{r}\right)\cdot\mathbf{n}dS + \phi_\infty \quad (1)$$

The Dirichlet boundary condition is applied at the collocation points to ensure the total inner potential with the freestream potential. The source strength is defined based on the tangency boundary condition, as the sum of the freestream velocity, the velocity induced by blade motions such as flapping, and the vertical component of the rotational velocity, as expressed in Eq. (2). The doublet intensity is calculated by the Kutta condition, which is the differences in doublet strength between the upper and the lower panels, as shown in Eq. (3).

$$\sigma = -(V_\infty + V_{rel} + \Omega \times r)\cdot n \quad (2)$$

$$\mu_{Wake} = \mu_{upper} + \mu_{lower} \quad (3)$$

The determined source and doublet strengths are distributed over each panel element. Then, by applying the Dirichlet boundary condition along with the influence coefficients due to the panel geometry, the formulation is expressed as shown in Eq. (4) (Ref. 13). Finally, the unknown doublet strength on the body surface is determined by solving the linear algebraic equation given in Eq. (5).

$$\sum_{k=1}^{N} A_{ik}\mu_k + \sum_{j=1}^{M_W} C_{ij}\mu_{W,j} + \sum_{k=1}^{N} B_{ik}\sigma_k = 0 \quad (4)$$

$$\begin{bmatrix} a_{11} & a_{12} & \cdots & a_{1N} \\ a_{21} & a_{22} & \cdots & a_{2N} \\ \vdots & \vdots & \ddots & \vdots \\ a_{N1} & a_{N2} & \cdots & a_{NN} \end{bmatrix} \begin{Bmatrix} \mu_1 \\ \mu_2 \\ \vdots \\ \mu_N \end{Bmatrix} = \begin{Bmatrix} RHS_1 \\ RHS_2 \\ \vdots \\ RHS_N \end{Bmatrix} \quad (5)$$

Afterward, the pressure coefficient at each panel's collocation point is obtained using velocity components in the discretized rotor blade and fuselage panels. Finally, Bernoulli's equation in Eq. (6) is applied to derive the pressure coefficient. For flow conditions with a Mach number above 0.3, the compressibility correction factor is applied to account for compressibility effects.

$$C_{P,0} = 1 - \frac{|V_{total}|^2}{|V_{kinematic}|^2} - \frac{2}{|V_{kinematic}|^2}\frac{\partial\phi}{\partial t} \quad (6)$$

3.2 Unsteady Vortex Particle Method

In the analysis of ground and obstacle effects, it is important to consider the effects of the wake generated by the rotor blade. In this study, the vortex particle method, which is the wake model of the VALOR solver, is employed to analyze the interaction between wake–wake, wake–fuselage, and wake–obstacle. The Lagrangian-based VPM represents wake behavior by tracking the position and velocity changes of vortex particles at each time step. Through an explicit time-marching scheme, each vortex particles propagate independently. This characteristic allows for the prediction of interactions between wake structures, such as wake-wake, rotor-fuselage, and rotor-obstacle interactions. The governing equation for the vortex field of the wake is expressed in Eq. (7), where v_i is the volume of the vortex particle, ξ_σ is a smoothing function, and $\mathbf{x}_i$ is the position of the particle.

(7) $$\omega(\mathbf{x},t)=\sum_{i=1}^{S}\xi_{\sigma}(\mathbf{x}-\mathbf{x}_i)\omega_i V_i$$

The intensity of each vortex particle is determined by the difference in doublet strength between the upper and lower surfaces, satisfying the Kutta condition. The induced velocity of each particle is calculated using the Biot–Savart law, as expressed in Eq. (8).

(8) $$u(\mathbf{x}_i,t)=\sum_{j=1}^{N}K_{\sigma}(\mathbf{x}_i-\mathbf{x}_j)\times\alpha_j$$

In this study, the dissipation effect of vorticity is not considered, and thus the core size of each vortex particle is kept constant throughout the simulation. Although there is a limitation in the methodology due to the absence of dissipation effects, the primary objective of this study is not to predict the far-field wake where dissipation plays a significant role. Instead, the focus is placed on capturing the near-field wake structure developed by ground and obstacle effects, and analyzing how this asymmetric wake affects the aerodynamic performance of the rotor blade.

4. Numerical setup

4.1. Validation

Before analyzing the unsteady aerodynamic loads and wake behavior of the UAM aircraft, two experimental studies were conducted to validate the numerical method under IGE conditions. First, the validation was performed using experimental data from Light's experiment on a four-bladed full-scale Lynx tail rotor hovering under IGE conditions (Ref. 3). The rotor consisted of four blades with the NPL 9615 airfoil and a constant chord length distribution without twist. Simulations were performed under both out-of-ground-effect (OGE) and IGE conditions, with H/R values of 1.54 and 0.84. Here, H represents the distance between the rotor hub and the ground.

Under IGE conditions, the thrust coefficient showed differences of 0.4%, 1.6%, and 0.7%, respectively, compared with the experimental data (Ref. 3). In addition, the Figure of Merit exhibited differences of 1.0%, 1.1%, and 2.5%, with the maximum deviation of 2.5%, indicating good agreement with the experimental results. Fig. 2 compares the radial and axial trajectories of tip vortices according to the rotor height above the ground. The positions of the vortex particles generated at the blade tips were tracked, and the experimental data and the numerical data were obtained using the vorticity transport model (VTM) (Ref. 15) and RANS (Ref. 16). As shown in Fig. 1, the result exhibit good agreement with the experimental data and other numerical models. Based on the predicted wake structure along the radial direction (X-axis) and the axial direction (Z-axis), the wake was initially contracted radially and then expanded again after impinging on the ground. In addition, the vertical development of the wake was limited by the ground surface. Through these experimental studies, the coupled vortex method used in this study is capable of predicting unsteady aerodynamic loads and wake behavior influenced by ground effect.

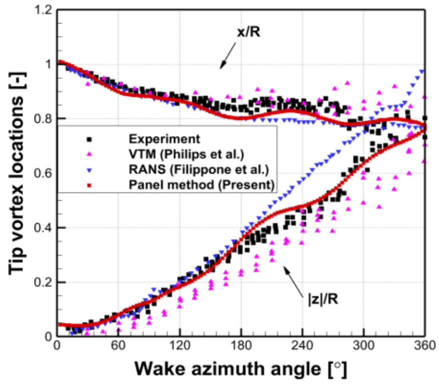

(a) OGE

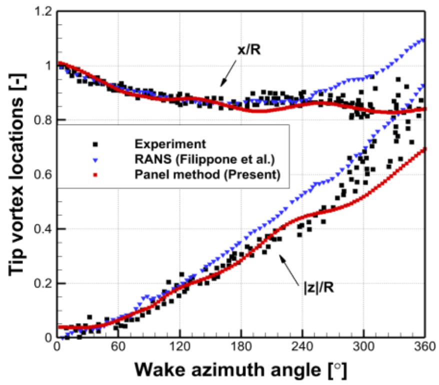

(b) IGE, H/R = 1.54

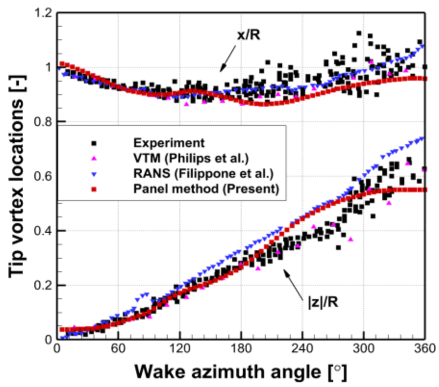

(c) IGE, H/R = 0.84

Figure 2: Tip vortex axial and radial locations of the Lynx tail rotor

Second, the validation was conducted under obstacle effects using the full configuration of the helicopter model. The validation model used in this study is derived from the Politecnico di Milano experiment helicopter model by Zagaglia (Ref. 17). Fig. 3 shows the test setup: the rotor, the fuselage, and the obstacle. The rotor model consists of four untapered, untwisted blades with a NACA 0012 profile. The rotor has a radius of 0.375 m and a chord length of 0.032 m. The detailed specifications and simulation conditions are presented in Table 1. The fuselage model is inspired by MD-500 fuselage. The ground was modeled as a 7 m X 5 m surface, and the obstacle was represented as a 0.8 m X 1.0m X 0.45m.

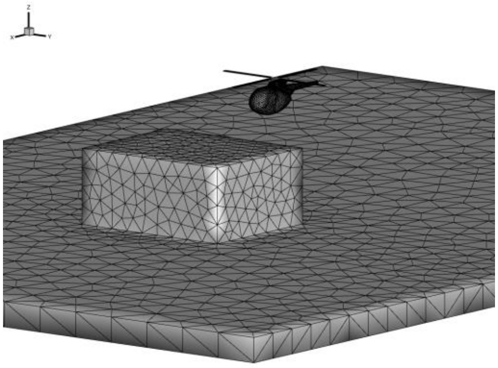

Figure 3: Geometry of the MD-500 helicopter model in the vicinity of the obstacle

Table 1: Specifications of the experiment rotor model and analysis conditions

Property	Value
Rotor radius	0.375 m
Chord length	0.033 m
Collective pitch angle	10°
Tip Mach number	0.286
Reynolds number	214,000
Time step	5°
Number of Grid (Chord & Span)	30/21
Number of Grid (Ground & Obstacle)	7295

The simulations were conducted under obstacle effect conditions at X/R = -1, -0.5, 0, 0.5, 1 with Z/R = 2.0. Fig. 4 compares the average thrust and torque of the rotor blades at different distances from the obstacle. The averaged thrust and torque results closely match with the experimental data (Ref. 17) and ROSITA CFD (Ref. 18), depending on the rotor position. At low Reynolds numbers, the Reynolds number scaling formulation was applied (Ref. 19). However, although the aerodynamic values at X/R = 1.0 were not precisely predicted, the overall results showed a similar trend. As a result, the panel method can predict unsteady aerodynamic loads under the ground and obstacle effects.

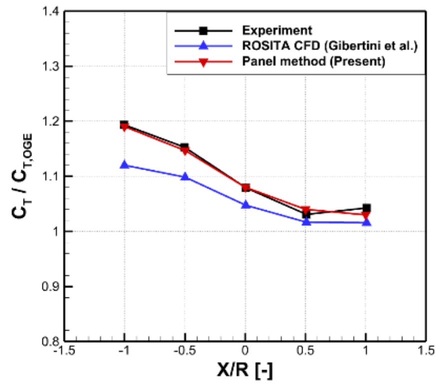

(a) Thrust coefficient

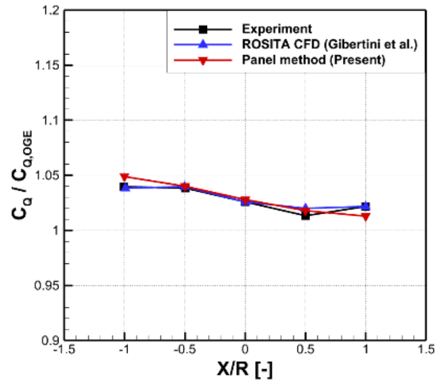

(b) Torque coefficient

Figure 4: Comparison of the thrust and torque coefficients of the rotor under IGE conditions

Fig. 5 presents a comparison of wake structures at various positions under the obstacle effects. Vortex particles generated at the blade tip formed an outwash region as they spread along the upper surface of the obstacle in all cases. In Fig. 5(a), the wake spreads in all directions over the top surface of the obstacle. The vortices then convected downstream along the obstacle side surface and spread again after impinging on the ground. Fig. 5(b) shows the asymmetric flow characteristics. On the right side of the rotor axis, a rapidly formed outwash region along the top of the obstacle surface. Meanwhile, on the left side of the rotor axis, vortex particles convect downstream, forming a recirculation region near the ground and the obstacle's edge. Based on this analysis, the wake model in this study is capable of capturing the wake distortion caused by the ground and obstacle effects.

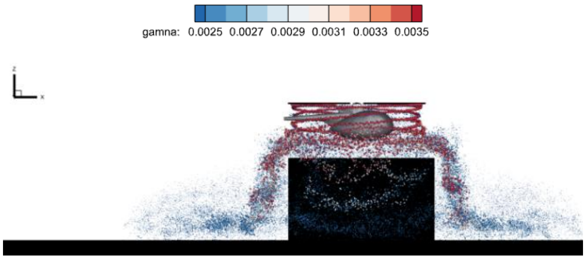

(a) X/R = -1.0

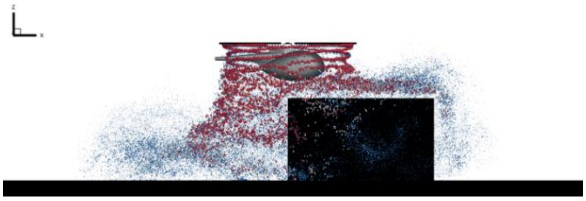

(b) X/R = 0.0

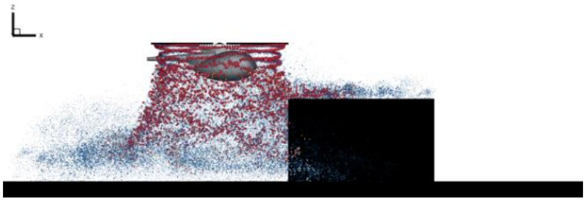

(c) X/R = 1.0

Figure 5: Comparison of the wake structure at various positions (Z/R=2.0)

4.2. Side-by-side eVTOL aircraft and obstacle

The UAM aircraft investigated in this study was a publicly available NASA OpenVSP model of SbS UAM vehicle (Ref. 20). Simulations include the left (clockwise) and right (counter-clockwise) rotors, as well as the fuselage without the landing gear. A phase shift of 45° was applied to the left rotor, and the relative rotor phasing was held constant. The separation distances between the hubs of two rotors for 15% overlap correspond to 1.7R, which is the best setup for efficiency (Ref. 21). Each rotor consists of four blades, with a rotor radius of 3.203 m and a tip chord length of 0.13 m. The rotor blades of SbS rotor were modeled based on two modern airfoils: Boeing VR-12 and Sikorsky SSC-A09. VR-12 was used at R < 85%, and the SSC-A09 was used for R > 95%. Linear interpolation between VR-12 and SSC-A09 was assumed for R > 85% and R < 95%. Additionally, 15° linear taper ratio was applied between R = 0.94 and the blade tip. Also, twist distribution was assumed to be linear, and detailed configurations and specifications are presented in Fig. 6 and Table 2.

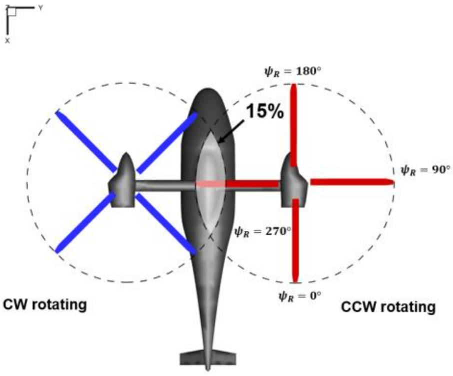

Figure 6: Definition of azimuth angle of SbS UAM aircraft with 15% overlap

Table 2: NASA Side-by-Side rotor specification

Property	Value
Number of rotors	2
Number of blades	4
Overlap ratio	15%
Rotor radius	3.203 m
Tip chord length	0.13 m
Tip Mach number	0.484
Collective pitch angle	12.2°

Each rotor blade is discretized into rectangular panel elements, with 30 panels in the chordwise direction and 31 panels in the radial direction. The surface grid for the SbS aircraft is shown in Fig. 7, where the fuselage is represented using 3,616 unstructured triangular source-doublet panels. To simulate an actual vertiport environment, the obstacle was modeled based on the FATO (Final Approach and Take-off Area) dimensions specified by the European Union Aviation Safety Agency (EASA) (Ref. 22). The ground plane and obstacle are resolved using 2,272 panels of 40m×55m and 18m×18m×10m in Fig. 8. To analyze the effects of obstacle, simulation was performed for 15 rotor revolutions, respectively, with a time step of 10 degrees.

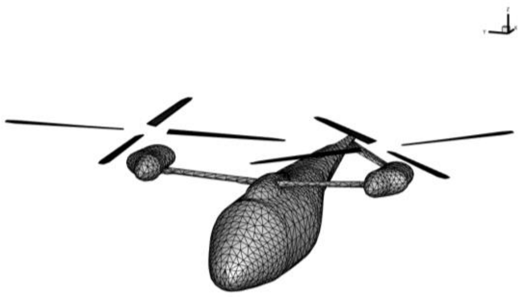

Figure 7: Surface grid of side-by-side UAM aircraft with 15% overlap

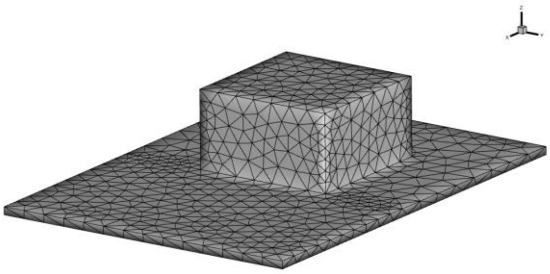

Figure 8: Surface grid of ground and obstacle plane

4.3. Numerical setup

Figure 9 and Table 3 present the test matrix for analyzing the obstacle effects. The origin of the global reference system is placed in the ground plane at the obstacle mid-span. The distance from the rotor hub to the ground or the obstacle is defined by the distance between the hub center and the reference origin. Based on this, the test matrix is defined by the distance between the rotor hub and the obstacle. Cases 1 to 3 were considered to investigate the obstacle effect during vertical take-off and landing conditions at X/R = −3.0, 0.0, and 3.0 with Z/R = 4.5. Additional conditions at X/R = -3.0, 0.0, and 3.0 with Z/R = 4.5 were considered to analyze the aerodynamics during the approach scenario.

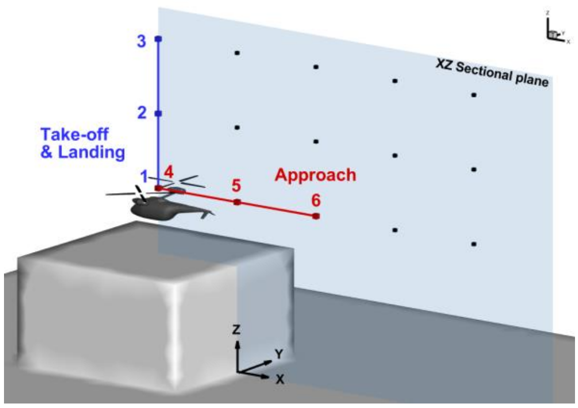

Figure 9: Location of SbS UAM aircraft

Table 3: Test matrix for investigating the obstacle effects

Test Case	X/R	Z/R	Sweep Axis
1	-3.0	4.5	Z
2	-3.0	5.5	Z
3	-3.0	6.5	Z
4	-3.0	4.5	X
5	0.0	4.5	X
6	3.0	4.5	X

5. Results and Discussion

5.1. Obstacle effect on SbS UAM aircraft during the vertical take-off and landing

Before analyzing the aerodynamics under the obstacle effects, the simulation model of the SbS UAM aircraft in full configuration was validated under the OGE condition, at a collective pitch angle of 8°. The thrust coefficient of the CFD analysis and that of the present study were 0.00667 and 0.00652, respectively, indicating good agreement (Ref. 21). This confirms that the present analysis model gives reasonable results.
To investigate the influence of obstacle effects on the aerodynamic performance of the SbS UAM aircraft, Cases 1 to 3 were defined along a vertical line on the symmetry plane at X = −3.0R. Fig. 10 presents a comparison of the maximum and minimum values of the thrust coefficient at various heights above the top surface of the obstacle. The highest average thrust was observed in Case 1, which was located closest to the obstacle surface. It was also observed that the thrust increased as the distance from the obstacle decreased. The thrust coefficient increased by up to 3.54% compared to case 3. It is indicated that the thrust increased due to the ground effect generated on the top surface of the obstacle. In addition, the difference between the maximum and minimum thrust values tended to increase as the aircraft approached the obstacle, with peak-to-peak variations of 6.3%, 4.1%, and 3.38%, respectively. These large percentage variations indicate that unsteady aerodynamic loads are acting on the rotor blades.

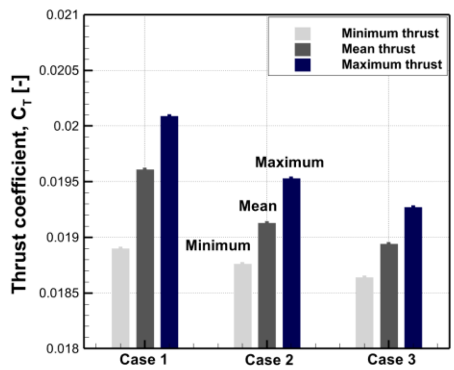

Figure 10: Comparison of mean thrust and peak-to-peak value along the heights

To analyze the unsteady aerodynamic loads acting on the rotor blades in more detail, Fig. 11 shows the aerodynamic load of the rotor blades in one revolution. Case 1 exhibited greater thrust oscillation compared to the other cases. Downwash generated by the rotor is reflected by the ground surface, forming a recirculation region and upward flow near the rotor disk. This leads to the unsteady aerodynamic loads, resulting in greater oscillation of the thrust coefficient. Interestingly, as the distance from the obstacle increased, the thrust became similar to that under the out-of-ground effect condition. In addition, when the distance from the obstacle exceeds Z/R = 5.5, the influence of the ground effect becomes minimal or negligible.

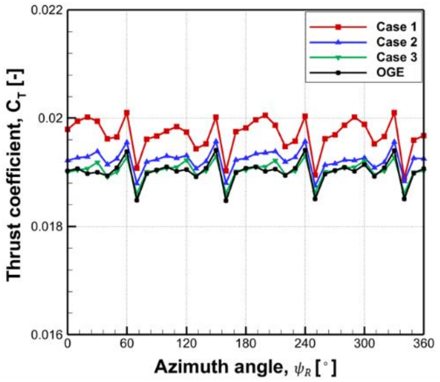

Figure 11: Time variation in thrust coefficient of SbS rotor for one rotor revolution

Figure 12 shows the thrust contour on the right rotor disk. For all cases, a reduction in thrust was observed at ψ = 270°, where the influence of the overlap effects becomes dominant (Ref. 11). As shown in Fig. 12(a), the impact of ground effect becomes more pronounced, as evidenced by the azimuthal distribution. Furthermore, the thrust distribution on the rotor plane shows asymmetry caused by the interaction between the rotor wake and the fuselage, and is further affected by the proximity to the obstacle. It was also confirmed that the thrust distribution on the rotor plane decreases as the distance from the obstacle increases. In particular, Fig. 19(c) shows a thrust contour similar to that observed under the OGE condition shown in Fig. 19(d).

The wake structure under the interaction of the ground and the obstacle at X = −3.0R is plotted in Fig. 13. A Clear interaction between the tip vortices from the left rotor and right rotor blades at the entrance and exit regions in all cases. It is shown that, at Z = 4.5R, Fig. 13(b), the rotor tip vortices first contract radially, and then expand as they impinge the top surface of the obstacle, covering the obstacle

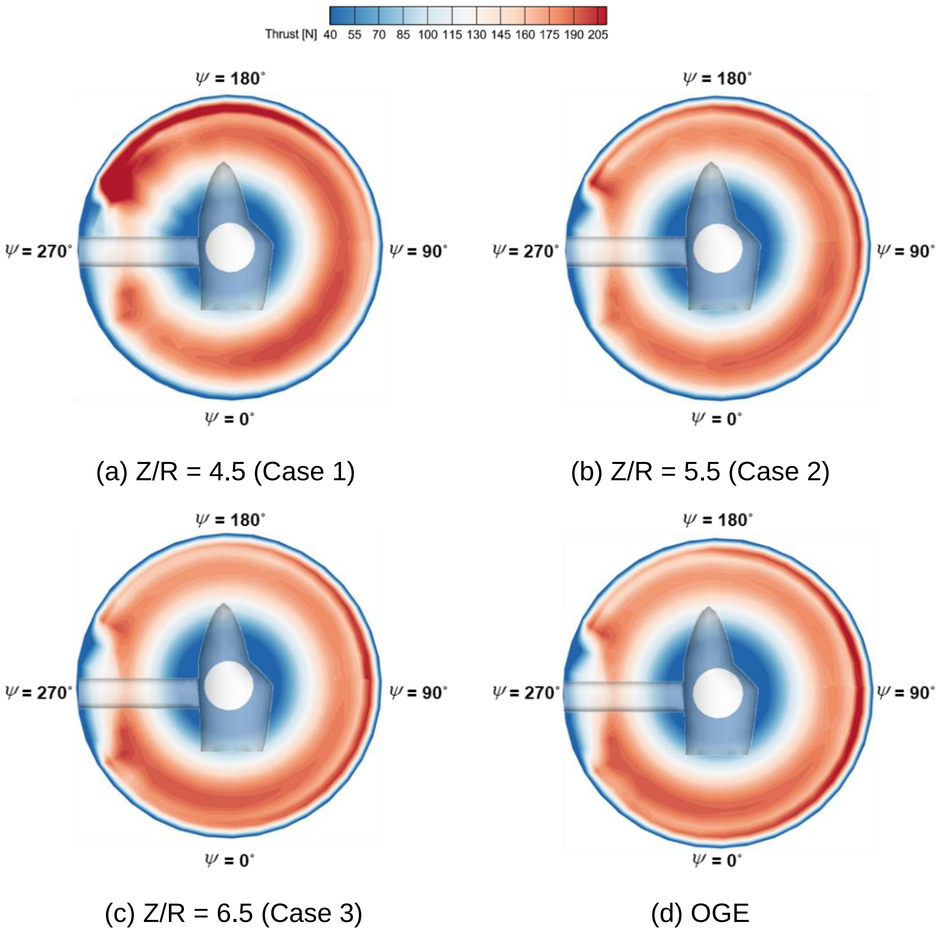

(a) Z/R = 4.5 (Case 1)

(b) Z/R = 5.5 (Case 2)

(c) Z/R = 6.5 (Case 3)

(d) OGE

Figure 12: Sectional thrust contour on the right rotor disk of SbS UAM in full configuration

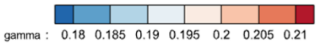

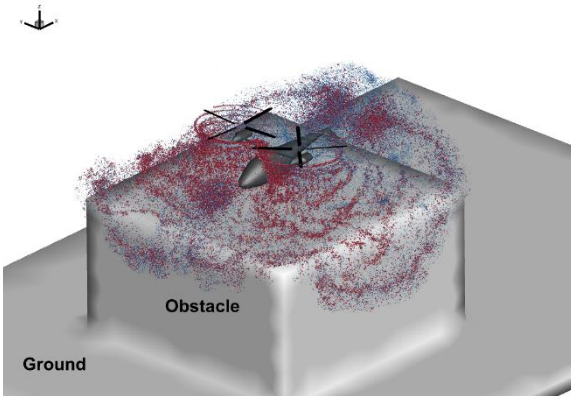

(a) Wake structure (Z/R = 4.5)

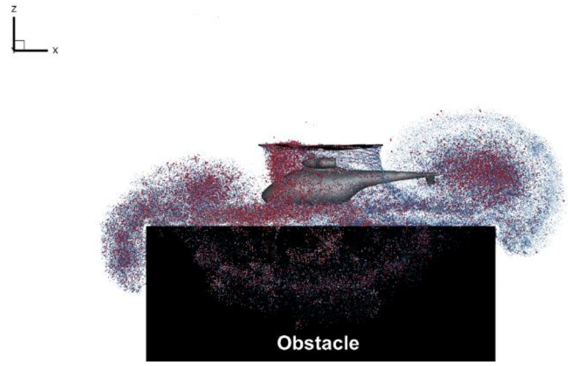

(b) Sectional wake structure in XZ plane (Z/R = 4.5)

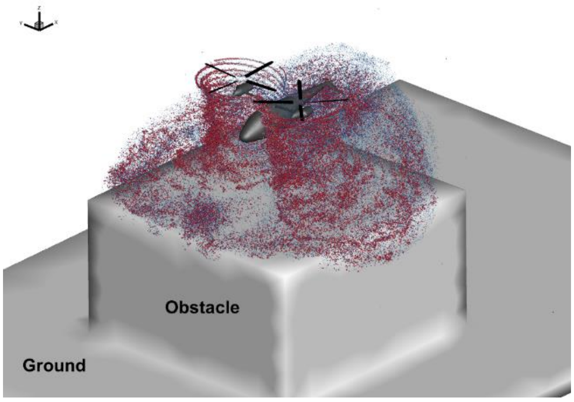

(c) Wake structure (Z/R = 5.5)

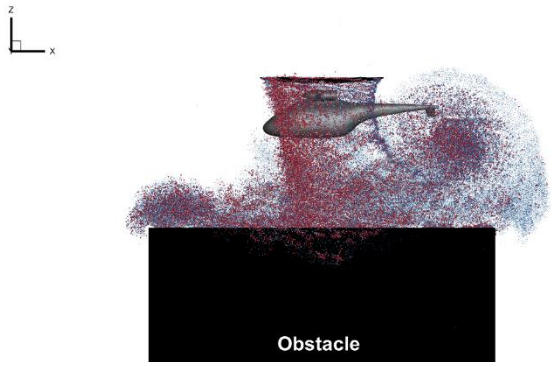

(d) Sectional wake structure in XZ plane (Z/R=5.5)

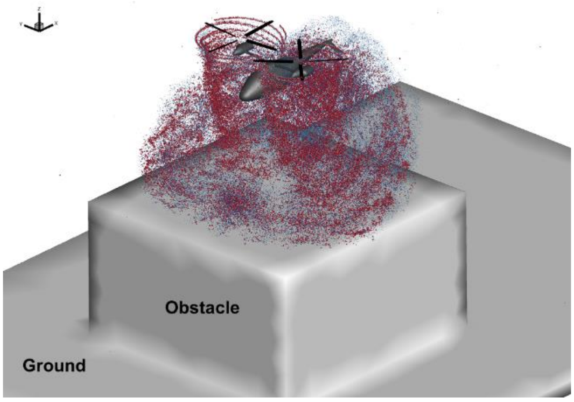

(e) Wake structure (Z/R = 6.5)

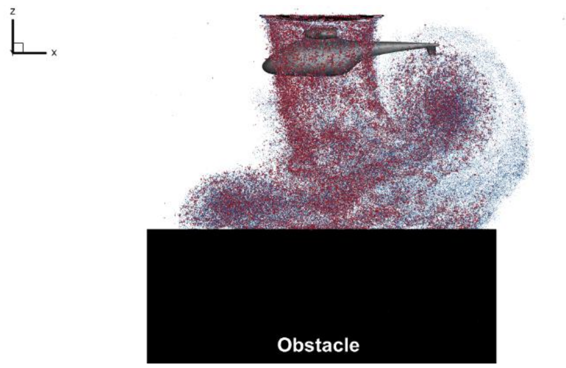

(f) Sectional wake structure in XZ plane (Z/R=6.5)

Figure 13: Comparison of wake evolution of SbS UAM aircraft under the obstacle effects at X/R = -3.0

surface. Furthermore, those vortices convect away from the four sides of the obstacle after impinging upon its top surface. A strong recirculation is formed in the downward direction due to the rotational direction. In addition, as the rotorcraft approaches the obstacle, strong interactions occur among the rotor, the fuselage, and the obstacle. This leads to a decrease in downwash velocity, increasing the thrust of the UAM aircraft. As the distance increases, the influence of the wake effects on the top surface of the obstacle becomes negligible. At Z/R = 6.5, where the aircraft is located far from the obstacle, the influence of the wake is still present above the obstacle. However, this wake structure is expected to be negligible when the dissipation of the vortex is taken into account.

Figure 14 shows the vertical velocity field of the SbS rotor in the XZ plane to analyze the wake behavior in more detail. As shown in Fig. 14(a), the downwash is significantly reduced due to the ground effect on the top surface of the obstacle. As the distance from the obstacle increases, the downwash generated by the rotor gradually increases. In all conditions, the recirculation region was observed where the vertical velocity rapidly changed from negative to positive. Fig. 14(a) shows more intense coloration, indicating a stronger recirculation region above the obstacle in the aft fuselage. In addition, it can be observed that the recirculation region is formed farther away.

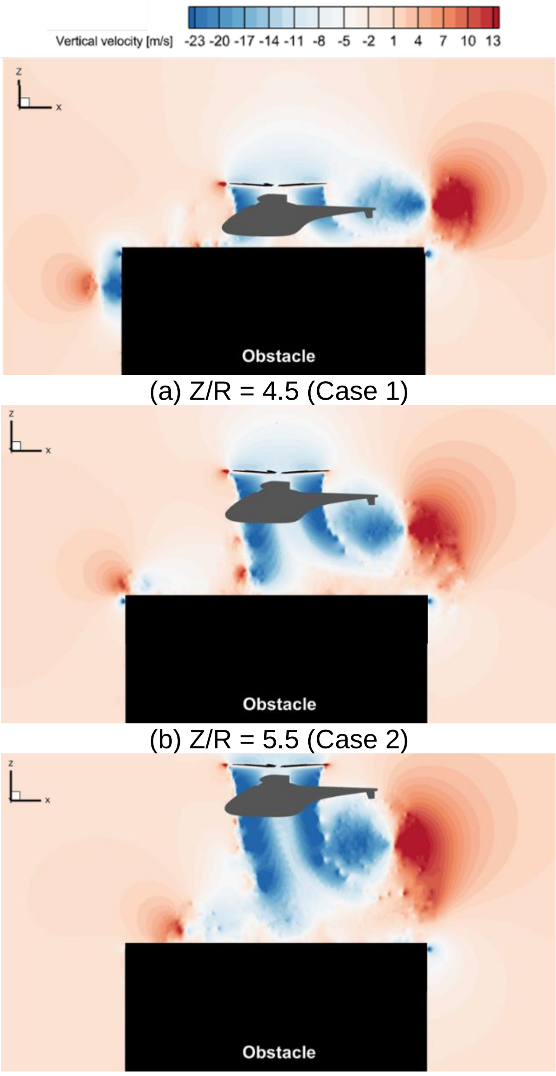

(a) Z/R = 4.5 (Case 1)

(b) Z/R = 5.5 (Case 2)

(c) Z/R = 6.5 (Case 3)

Figure 14: Comparison of the instantaneous vertical velocity contour of SbS UAM aircraft under the obstacle effects at X/R = -3.0

5.2. Obstacle effect on SbS UAM aircraft during the approach

To investigate the obstacle effect on aerodynamics and wake behavior of a SbS UAM aircraft during the approach scenario, Cases 4 to 6 defined in Table 3 were compared. Fig. 15 shows the comparison between the maximum and minimum values of the thrust coefficient hovering above the obstacle, depending on the distance from the obstacle. As expected, the mean thrust was highest in Case 4 when the entire rotor disk was over the obstacle. Compared to Case 6, which is similar to the OGE condition, the mean thrust increased by up to 3.5%. This is because the wake impinges on the ground and forms a recirculation region, which reduces the induced velocity and increases the effective angle of attack, resulting in increased thrust. This result shows that a ground effect similar to the one on a flat ground was also generated above the obstacle. As the distance from the obstacle decreased, both the average thrust and the peak-to-peak value increased with peak-to-peak variations of 6.3%, 4.53%, and 3.84%, respectively. The influence of the ground effect became negligible at X/R greater than 3.0.

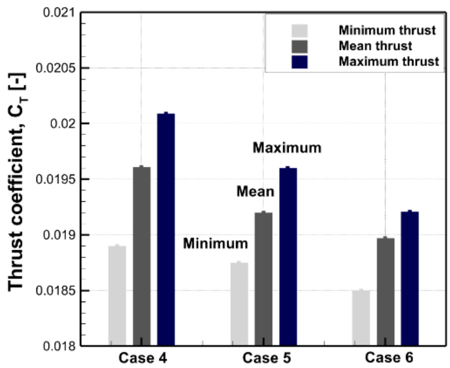

Figure 15: Comparison of averaged thrust and peak-to-peak value along the distance

To analyze the thrust variation in more detail, Fig. 16 shows the aerodynamic load of the rotor blades in one revolution. As expected, the mean thrust increases as the aircraft approaches the obstacle. As shown earlier in Fig. 15, the thrust oscillation shows a slight variation in Cases 4 and 5 compared with that in Case 6. Case 4 showed the highest thrust and fluctuation due to the strong interaction between the rotor wake and the obstacle.

Multiple interactions were manifested on the right rotor disk, as shown in the thrust contour of Fig. 17. Rapid variation in loading distribution was observed in the overlapping region between the rotors, with significant impulsive changes at the entrance (ψ =

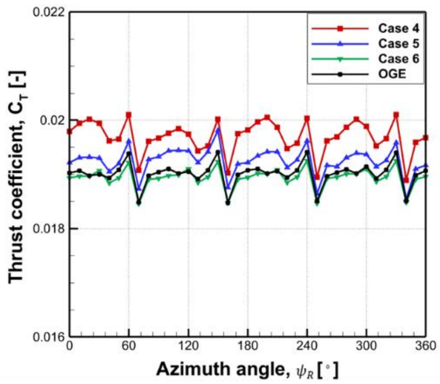

Figure 16: Time variation in thrust coefficient for one rotor revolution under IGE conditions

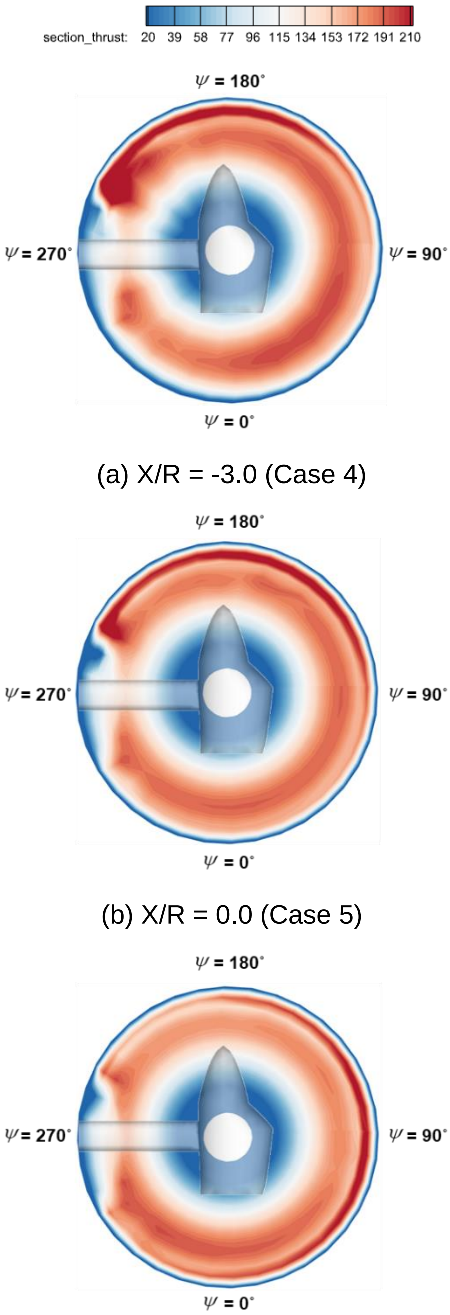

(a) X/R = -3.0 (Case 4)

(b) X/R = 0.0 (Case 5)

(c) X/R = 3.0 (Case 6)

Figure 17: Sectional thrust contour on the right rotor disk of full configuration

225°) and exit (ψ = 315°) of the overlapped area on the right rotor. In this region, the dominant interaction is the tip vortices from one rotor with the other rotor, notably near the exit and entrance regions of the rotor overlap (Ref. 21). As the rotorcraft moves closer to the obstacle, higher upwash is observed across the rotor plane compared to Case 6. In the case of Fig. 17(b), where the rotor disk is positioned over half of the obstacle, an increase in thrust was observed in the forward region of the rotor plane due to upwash. Also, the rotor disk above the half of the obstacle shows increased thrust, while the other half is not affected by ground effect, resulting in an asymmetric thrust distribution.

To investigate the effect of the obstacle on the wake behavior of the aircraft in more detail, wake structure and vertical velocity contour were analyzed in Fig. 18 and Fig. 19. Strong vortices were developed behind the rotorcraft in all cases. As the rotorcraft moves closer to the obstacle, the center of recirculation moves farther from the rotor centroid. In addition, the strength of the recirculation region increased near the forward and aft fuselage as the rotorcraft approached the obstacle. This was also shown in the vertical velocity field in Fig. 19, where the strongest upwash was observed in Case 1 above the obstacle. It is shown that, at X/R = -3.0, Figs. 18(a) and (b), the rotor tip vortices first contract radially and then expand as they approach the top surface of the obstacle, and wrap around the obstacle. The recirculation region in the forward fuselage moved downward along the side of the obstacle surface, resulting in a decrease in its strength. Figs. 18(c) and (d) show the condition where the rotor is located at the middle position above the obstacle. Asymmetric flow characteristics were observed on both sides of the centroid of the rotors. The wake generated on the left side of the roto axis was divided into two directions on the upper surface of the obstacle. The wake spreading to the left formed outwash along the obstacle surface. In contrast, the wake on the right side of the rotor axis convects downstream along the side surface of the obstacle. An increase in downwash velocity along the obstacle side surface was observed in Fig. 19(b). In Figs. 18(f) and 19(c), it was observed that the wake was not influenced by the presence of the obstacle. As the distance between the rotor and the obstacle increases,

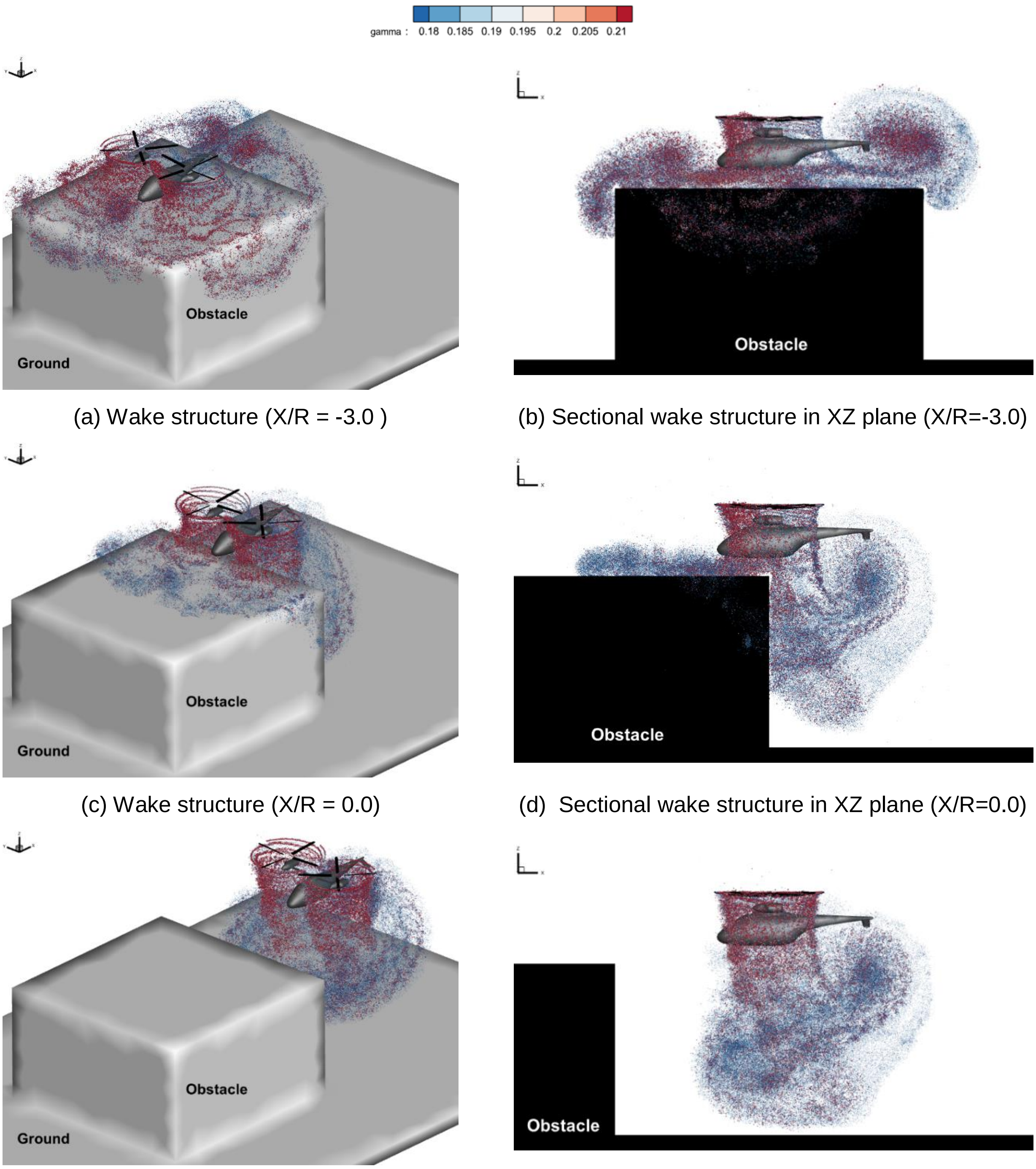

(a) Wake structure (X/R = -3.0)

(b) Sectional wake structure in XZ plane (X/R=-3.0)

(c) Wake structure (X/R = 0.0)

(d) Sectional wake structure in XZ plane (X/R=0.0)

(e) Wake structure (X/R = 3.0)

(f) Sectional wake structure in XZ plane (X/R=3.0)

Figure 18: Comparison of wake evolution of SbS UAM aircraft under the obstacle effects at Z/R = 4.5

the influence of the wake on the obstacle becomes negligible. At X/R = 3.0 or higher, the wake propagates only downstream and is no longer affected by the obstacle effect.

5.3. Aerodynamic variation under obstacle effects

Based on Cases 1 to 6, the effect of the obstacle on the aerodynamic performance, wake structure, and vertical velocity field of the UAM aircraft was analyzed. To further investigate the obstacle effects on the thrust variation of a UAM aircraft, aerodynamic

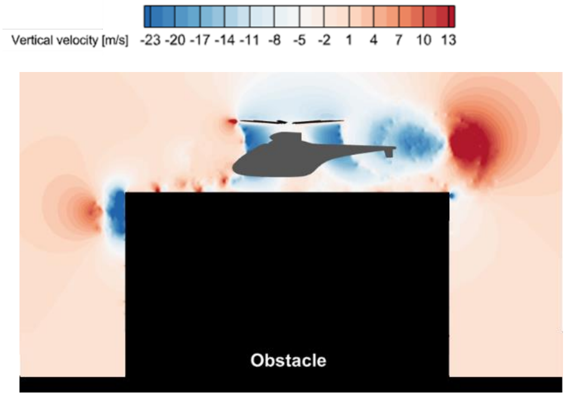

(a) X/R = -3.0 (Case 4)

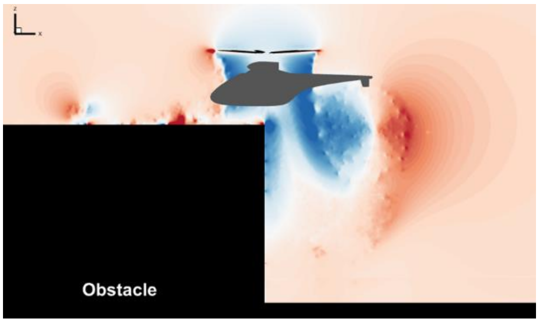

(b) X/R = 0.0 (Case 5)

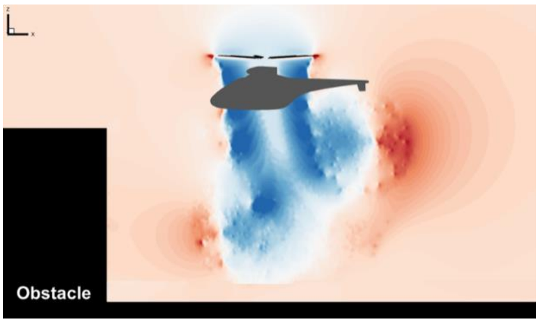

(c) X/R = 3.0 (Case 6)

Figure 19: Comparison of the instantaneous vertical velocity contour of SbS UAM aircraft under the obstacle effects at Z/R = 4.5

analysis was additionally performed at 9 locations beyond the 6 previously analyzed positions. Fig. 20 shows the thrust ratio relative to the OGE condition at 15 aircraft positions selected based on variations in height (Z/R) and distance (X/R) from the obstacle. Based on the thrust distribution shown in Fig. 18, it was confirmed that the thrust increased above the obstacle due to the ground effect. At the top of the obstacle (X/R = –3.0), where the highest thrust was observed, comparison between Z/R = 4.5 and Z/R = 7.5 showed that thrust increased by up to 2.5 percent as the rotor was positioned closer to the obstacle. When the UAM aircraft was positioned above the obstacle, the overall thrust increased compared to the positions beyond the obstacle at X/R > 0. These results indicate that the obstacle effect becomes most dominant either when the aircraft is located above the obstacle or when the distance to the obstacle decreases.

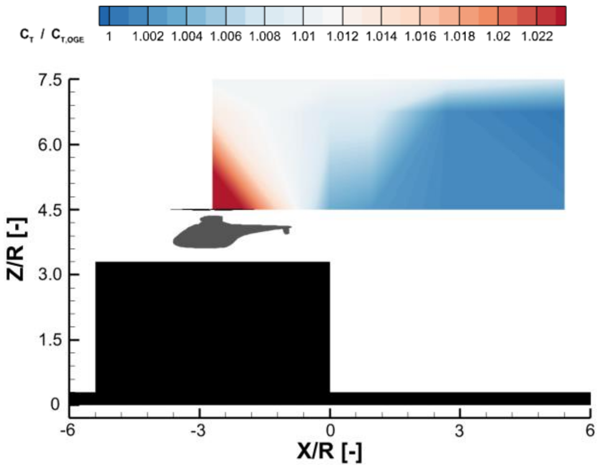

Figure 20: Contour of the thrust ratio at various positions

6. CONCLUSIONS

This study investigates the obstacle effects on the aerodynamics and wake structure of NASA's side-by-side UAM aircraft in full configuration using a vortex-based rotorcraft analysis software code, VALOR (Vortex-based Aerodynamic simuLation cOde for Rotorcraft). Six cases were considered to investigate the obstacle effect: three vertical take-off and landing cases at Z/R = 4.5, 5.5, and 6.5 with X/R = -3.0, and three approach cases at X/R = −3.0, 0.0, and 3.0 with Z/R = 4.5. The obstacle effects on aerodynamics at various positions are discussed below.

1. During the vertical take-off and landing, the mean thrust increases due to the ground effect generated on the top surface of the obstacle. The thrust coefficient increased by up to 3.54% compared to the farthest case. Additionally, the peak-to-peak variations in thrust became larger near the obstacle, indicating stronger unsteady aerodynamic loads on the rotor blades.

2. As the rotorcraft approaches the obstacle, interactions among the rotor, fuselage, and obstacle reduce the downwash velocity, resulting in increased thrust. With increased distance, the wake effect on the obstacle surface diminishes and becomes negligible beyond Z/R = 6.5.

3. During the approach, the thrust increased by up to 3.5% compared to the OGE condition as the

distance to the obstacle decreased. This is because the obstacle surface, similar to the ground, reduced the induced velocity and increased the effective angle of attack.

4. As the rotorcraft approached the obstacle, strong recirculation and upwash were formed near the forward and aft aircraft. The rotor tip vortices contracted rapidly and then expanded around the obstacle, showing asymmetric wake structure around the centroid of the rotor axis.
5. The aerodynamic performance of a side-by-side UAM aircraft under obstacle effects was analyzed at 15 locations for parametric studies. The results showed that thrust increased above the obstacle due to partial ground effect. The maximum thrust was observed at the top edge of the obstacle when the rotor was positioned closer. These findings indicate that the obstacle effect becomes most dominant when the aircraft is near or above the obstacle.

In this study, the aerodynamic performance and wake behavior of a UAM aircraft near an obstacle were analyzed. However, the effect of wake particle dissipation due to viscous diffusion was not considered. In future work, analysis will be performed with wake dissipation included, and the obstacle effect will be investigated for various UAM configurations beyond the SbS UAM aircraft.

Author contact:

Chan Ho Song chanho0507@gnu.ac.kr

Sang Min Son 2017011848@gnu.ac.kr

Da-bin Jung jbin8226@gnu.ac.kr

Rho Shin Myong myong@gnu.ac.kr

Hakjin Lee hlee@gnu.ac.kr

7. ACKNOWLEDGMENTS

This work was supported by the National Research Foundation of Korea (NRF) grant funded by the Korea government (MSIT) (RS-2024-00397400). This work was supported by the Glocal University 30 Project Fund of Gyeongsang National University in 2025.

8. REFERENCES

1. Wadcock, A., Ewing, L., and Solis, E. et al., “Rotorcraft Downwash Flow Field Study to Understand the Aerodynamics of Helicopter Brownout," AHS Southwest Region Technical Specialists Meeting, Dallas, TX, Oct 2008.
2. Laurie A. G., Brian J. G. and Caroline E. L et al. “Urban air mobility: A comprehensive review and comparative analysis with autonomous and electric ground transportation for informing future research,” Transportation Research Part C 132, 2021.
3. Light, J. S., “Tip Vortex Geometry of a Hovering Helicopter Rotor in Ground Effect,” *Journal of the American Helicopter Society*, Vol. 38, No. 2, 1993, pp. 34-42.
4. T. E. Lee, G. J. Leishman, and M. Ramasamy, “Fluid Dynamics of Interacting Blade Tip Vortices with a Ground Plane,” *Journal of the American Helicopter Society*, Vol. 55, No. 2, 2010, 22005-1-22005-16.
5. Glauert, M. B., “The Wall Jet,” *Journal of Fluid Mechanics*, Vol. 1, (6), 1956, pp. 625-643.
6. D. Zagaglia, M. Guini, and R.B. Green, “Investigation of the Rotor-Obstacle Aerodynamic Interaction in Hovering Flight,” *Journal of the American Helicopter Society*, Vol. 63, 2018, 032007 (12 pages).
7. Tanner, P. E., et al., “Experimental Investigation of Rotorcraft Outwash in Ground Effect,” NASA Technical Report NASA/TM-2011-217104, 2011.
8. Zagaglia, D., Giuni, M., and Green, R. B., “Rotor-Obstacle Aerodynamic Interaction in Hovering Flight: An Experimental Survey,” AHS 72nd Annual Forum and Technology Display, West Palm Beach, FL, USA, 17-19 May 2016.
9. G. Chirico, D. Szubert, and G.N. Barakos et al., “Numerical Modelling of the Aerodynamic Interference Between Helicopter and Ground Obstacles,” *CEAS Aeronautical Journal*, Vol. 8, N. 4, 2017, pp. 589-611.
10. Renzoni, P. "GARTEUR: Nearly Half a Century of European Collaboration in Aeronautics," Proceedings of the 33rd Congress of the International Council of the Aeronautical Sciences (ICAS), Stockholm, Sweden, September 4-9, 2022.

11. J. Sagaga, S. Lee, “Acoustic predictions for side-by-side rotor with ground effect,” Proceedings of the 79th Annual Forum of the Vertical Flight Society, West Palm Beach, Florida, 2023.
12. Araghizadeh, M. S., Sengupta, B., Lee. H, Myong. R.S., “Aeroacoustic Investigation of Side-by-side Urban Air Mobility Aircraft in Full Configuration with Ground Effect,“ *Physics of Fluids*, Vol. 36, No. 8, 087160, 2024. 08.
13. Katz, J., and Plotkin, A., “Low Speed Aerodynamics,” 2nd Edition, *Cambridge University Press*, 2001.
14. Lee, H. J., Sengupta, B., Araghizadeh, M. S., and Myong, R. S., "Review of vortex methods for rotor aerodynamics and wake dynamics," *Advances in Aerodynamics* 4.1, 2022.
15. Philips, C., Kim H. W., and Brown, R.E., “The Flow Physics of Helicopter Brownout,” Proceedings of the 66th American Helicopter Society Forum: Rising to New Heights in Vertical Lift Technology, Fairfax, VA, 2010.
16. Filippone, A., et al., “Rotor Wake Modelling in Ground Effect Conditions,” Proceedings of the 37th European Rotorcraft Forum, Vergiate and Gallarate, Italy, 2011.
17. G. Gibertini, D. Grassi, C. Parolini, D. Zagaglia, and A. Zanotti. “Experimental investigation on the aerodynamic interaction between a helicopter and ground obstacles,” Proceedings of the Institution of Mechanical Engineers, Part G: Journal of Aerospace Engineering. 1395-1406. 2015.
18. Chirico G., Gennaretti M., and Bernardini G. et al., “Experimental investigation on the aerodynamic interaction between a helicopter and ground obstacles,” *Aerospace Science and Technology*, Volume 78, pp. 167-179, 2018.
19. Keys, C. N., McVeigh, M. A., Dadoane, L., et al., “Estimation of Full-Scale Rotor Performance from Model Rotor Test Data,” *Journal of the American Helicopter Society*, Vol. 30, No. 4, 1985.
20. Litherland, B., and Holland, S., “NASA Urban Air Mobility (UAM) Reference Vehicle,” National Aeronautics and Space Administration.
21. Sagaga, J., and Lee, S., “High-fidelity computational study of aerodynamic noise of side-by-side rotor in full configuration,” *Journal of Sound and Vibration*, Vol. 592, p. 118607, 2024.
22. European Union Safety Agency, Prototype Technical Specifications for the Design of VFR Vertiport for Operation with Manned VTOL-Capable Aircraft Certified in the Enhanced Category. Vertiport, PTS-VPT-DSN, Cologne, Germany, March 2022.